Int J CARS (2009) 4:181–188
DOI 10.1007/s11548-008-0281-y

REVIEW ARTICLE

Combining a deformable model and a probabilistic framework for an automatic 3D segmentation of prostate on MRI

Nasr Makni · P. Puech · R. Lopes · A. S. Dewalle · O. Colot · N. Betrouni

Received: 10 January 2008 / Accepted: 29 October 2008 / Published online: 3 December 2008

Abstract
Purpose Accurate localization and contouring of prostate are crucial issues in prostate cancer diagnosis and/or therapies. Although several semi-automatic and automatic segmentation methods have been proposed, manual expert correction remains necessary. We introduce a new method for automatic 3D segmentation of the prostate gland from magnetic resonance imaging (MRI) scans.
Methods A statistical shape model was used as an a priori knowledge, and gray levels distribution was modeled by fitting histogram modes with a Gaussian mixture. Markov fields were used to introduce contextual information regarding voxels' neighborhoods. Final labeling optimization is based on Bayesian a posteriori classification, estimated with the iterative conditional mode algorithm.
Results We compared the accuracy of this method, free from any manual correction, with contours outlined by an expert radiologist. In 12 cases, including prostates with cancer and benign prostatic hypertrophy, the mean Hausdorff distance and overlap ratio were 9.94 mm and 0.83, respectively.
Conclusion This new automatic prostate MRI segmentation method produces satisfactory results, even at prostate's base and apex. The method is computationally feasible and efficient.

N. Makni (✉) · P. Puech · R. Lopes · A. S. Dewalle · N. Betrouni
Inserm, U703, ITM, Pavillon Vancostenobel,
CHRU Lille, 59037 Lille, France
e-mail: nasr.makni@gmail.com

N. Makni · R. Lopes · O. Colot
LAGIS, CNRS, UMR 8146, USTL,
59655 Villeneuve d'Ascq, France

P. Puech
Radiology Department, University Hospital Lille, Lille, France

Keywords Prostate cancer · Segmentation · 3D deformable model · Markov fields

Introduction

In the last decade, magnetic resonance imaging (MRI) examinations have been a reference in prostate cancer extension assessment, and were carried out when the tumor had already been diagnosed by biopsy. On the other hand, ultrasound imaging (US) and computed tomography (CT) scans are widely used in prostate segmentation applications, such as interventional procedures [1], where real-time aspect is an undeniable advantage of US. CT scans are also commonly used for prostate and other organs-at-risk delineation, for treatment planning of prostate cancer radiotherapy, as Pekar et al. [2] and Chaney et al. [3] suggested. Recently, there has been a growing interest in MR prostate imaging for guided biopsies, treatment planning of robotized surgery, and for emerging focal cancer ablation techniques (HIFU, photodynamic or thermal therapy, etc.). In these cases, MRI is best suited as its soft tissue contrast is superior to CT scan images and ensures better delineation of the prostate, particularly of the apex and seminal vesicles [4,5]. Prostate volume on MRI appears to be from 27 to 40% smaller than on CT and inter-observer variation of apex location is reduced [6,7]. It also provides a better contrast resolution for intragland tissue characterization, and allows full 3D description of the gland, potential regions of interest, and surrounding structures. Some authors have stated that MRI alone could be used in prostate cancer radiotherapy treatment planning [8,9]. Considering this emerging role of MRI, and keeping in mind that prostate manual delineation is a time-consuming task, the development of automated prostate segmentation tools has become a critical issue. Various image processing

techniques have been investigated: Mazonakis et al. [10] presented a growing region-based technique for prostate, bladder and rectum segmentation on CT images, in which user intervention remains necessary for thresholds definition. In a recent work, Klein et al. [11] proposed an automatic prostate segmentation method based on non-rigid registration of a set of pre-labeled MR atlas images. We could notice that organ model-based methods are widely used in prostate delineation. Freedman et al. [12] combined an appearance model with probability distribution of object-inside photometric variables for prostate and rectum segmentation. El Naqa et al. [13] have developed variational methods based on multi-valued level set deformable models for simultaneous 2D or 3D segmentation of multimodality images consisting of combinations of co-registered PET, CT, or MR data sets. In a recent work, Costa et al. [14] proposed a method for 3D localization and segmentation of prostate and bladder CT images, using coupled 3D deformable models. In 2007, Pasquier et al. [15] presented a deformable model-based method for automatic prostate volume definition in conformal radiotherapy planning MRI images. The authors have established a statistical 3D shape model (SSM) [16] that is deformable to fit prostate's contours. This method globally showed good results, but manual correction was still necessary for both apex and base of the gland, where contrast between prostate and surrounding structures (muscles and seminal vesicles, respectively) is a challenging issue. In this article, we refine results obtained by Pasquier et al. by introducing the same SSM in a Bayesian classification framework. The use of Markov fields allows us to combine contextual information on voxels' neighborhood and gray levels with a priori knowledge on the gland's geometry.

Method

We consider two random fields $X = \{x_s, s \in S\}$ and $Y = \{y_s, s \in S\}$, where S is the set of voxels.

Each x_s takes its values in a finite set of labels $\Omega = \{-1, 1\}$ and each y_s takes its value in the set of MRI levels.

The approach described in this paper is a Bayesian segmentation that can be summarized in four steps:

(i) Integration of prostate 3D model that will be used as an initial labeling X^0.
(ii) Characterization of an a priori probability $P(X)$ of voxels' labeling, using Markov field modeling.
(iii) Establishment of a conditional law for the image gray levels $P(Y|X)$.
(iv) Estimation of the optimum labels' field X that maximizes the a posteriori probability $P(X|Y)$.

Figure 1 shows the organizational structure of the method.

3D model

In a previous work [17,18], a generic prostate model had been established from a training base of 20 manual outlines. The statistical shape model [16,19], deduced by a principal component analysis (PCA), is composed of an average shape and the most important deformation directions. Depending on the thickness, size and shape of slices, the prostate often appears on 8–12 slices in standard pelvic MR examination. To get a 3D model, the prostate was contoured, on each slice, by placing 20 points represented by their 3D coordinates $p_i = (x_i, y_i, z_i)$. Thus, the prostate surface is modeled by a vector $X = [x_0, y_0, z_0, x_1, y_1, z_1 \ldots, x_P, y_P, z_P]$, where P is the total number of surface points. For this study, whatever the number of slices used, the total number of prostate points P was brought to 200. Twenty points were used to describe each 2D contour as a compromise between the time spending and a detailed description of the contour variation. It should be underlined that this number of points is higher than the number of points usually laid out by the experts for delineating the prostate for radiotherapy purposes.

We initialize this SSM on the images, and a heuristic optimization by simulated annealing algorithm is performed to estimate parameters that best describe prostate's contours, as detailed in [20]. This first 3D contour is converted into a set of labels by attributing +1 to voxels that belong to prostate

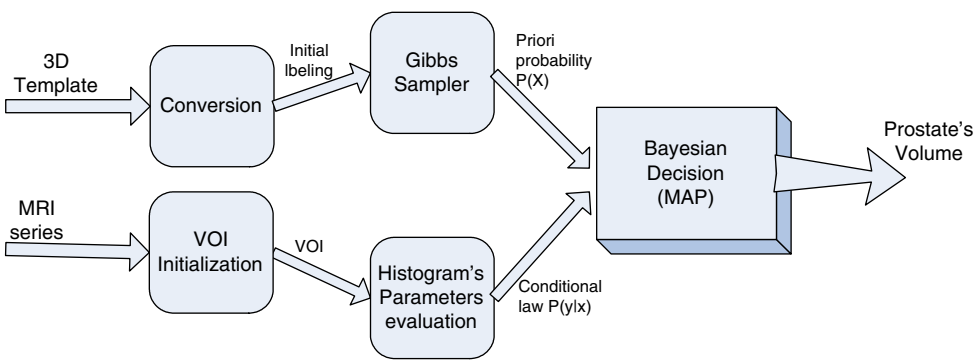

Fig. 1 Global scheme of the method

and -1 to those that do not. Consequently, an initial labels' vector X^0 is established.

A priori probability

The initial labeling X^0 cannot be operated without ensuring that it performs a Markov field. Precisely, according to Hammersley–Clifford's theorem (1971) for which a demonstration is given in [21], X is a Markov field if and only if it follows a Gibbs' distribution, defined as follows:

$$P(x) = \frac{1}{Z}\exp[-U(x)] \tag{1}$$

$$U(x) = \sum_{c\in C} J_c(x_c) \tag{2}$$

where J_c is a clique-related potential that will be defined further on, X_c is the restriction on the clique c, and C is the set of S cliques.

To meet this requirement, we use the Gibbs' sampler algorithm. Frequently cited in the literature [22], it can generate a Markov field from any vector of labels. To do this, we have to express the a priori probability $P(X)$ by defining the energy function $U(x)$. We will then use Potts' (or Ising) model [23] which defines $U(x)$ as

$$U(x) = -\beta\sum_{s\in S} x_s - \alpha\sum_{s\in S} x_s\left(\sum_{t\in V_s} x_t\right) \tag{3}$$

Evaluation of parameters α and β is usually carried out by estimation methods and fairly generic approximations [21]. In this work, we try to approach these parameters through simulation, as we have a relatively relevant initialization of the X field. We consider a 26-connexity system, in which the labels' sum in each voxel's neighborhood takes a value ranging $[-27, 27]$. Figure 2 shows the variation of $P(x_s = 1|x_{V_s})$ for different values of α and $\beta = 0$:

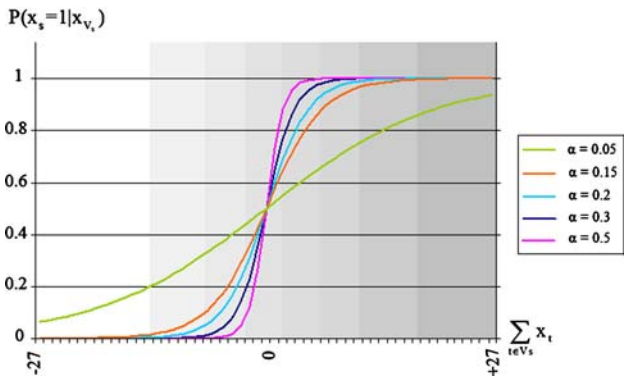

Fig. 2 A priori probability simulation

$$P(x_s = 1|x_{V_S}) = \frac{\exp[-U(1,x_{V_S})]}{\sum_{\omega\in\{-1;1\}}\exp[-U(\omega,x_{V_S})]}$$

$$= \frac{\exp[\alpha\sum_{t\in V_S} x_t]}{\sum_{\omega\in\{-1;1\}}\exp[\alpha\omega\sum_{t\in V_S} x_t]} \tag{4}$$

From simulation results we can establish that $P(x_s = 1|x_{V_s})$ becomes more "fuzzy" when α decreases; assigning a tiny value to α allows having a less deterministic labeling, which authorizes further evolution possibilities.

Image formation law

To model $P(Y|X)$, we conduct a statistical study on gray levels. We process the histogram in a volume of interest (VOI) defined as follows: at first the user defines a rectangle that surrounds prostate in a central slice; then he/she selects both upper and lower MRI slices. We can then define a 3D box by applying the central rectangle to all images located between upper and lower slices. This new field of view contains the gland and the surrounding tissues and allows us to avoid processing extra MRI data, without having any effect on segmentation results. Once we compute the histogram, we fit by a Gaussian mixture, which parameters are automatically extracted using a mode recognition algorithm [24]. We can then detect three modes:

(i) The first mode, which mean is located in the black levels, represents tissues and fat surrounding the prostate. In our study, we make it correspond to the class $\omega = -1$, and we compute its Gaussian parameters μ_{-1} and σ_{-1}.
(ii) The second mode represents the gray levels of prostate's central zone. We characterize it by its Gaussian parameters μ_{11} and σ_{11}.
(iii) The last mode is situated in the high gray levels, and represents peripheral zone texture and eventually some cysts in the transition zone. We characterize it by its Gaussian parameters μ_{12} and σ_{12}.

These two last modes are both representative of prostate tissues and correspond to the class $\omega = 1$, which could involve an ambiguity if we try to represent each class $\omega \in \{-1, 1\}$ by a single Gaussian mode.

So as a first approach, we approximate the conditional probability by

$$\begin{cases} P(y_s|x_s = \omega) = \frac{1}{Z_y}\cdot\frac{1}{\sqrt{2\pi}\sigma_\omega}\exp\left[-\frac{1}{2}\left(\frac{y_s-\mu_\omega}{\sigma_\omega}\right)^2\right] \\ \omega \in \{-1, 1\} \end{cases} \tag{5}$$

where Z_y is a normalization constant, and $(\mu_\omega, \sigma_\omega)$ are Gauss parameters of class ω. Then we select the mode that represents best the class $\omega = 1$ by comparing Mahalanobis distances between voxel gray level y_s and the two means μ_{11} and μ_{12}:

$$(\mu_1, \sigma_1) = \arg\left[\min_{i\in\{1,2\}}\left(\frac{y_s-\mu_{1i}}{\sigma_{1i}}\right)^2\right] \quad (6)$$

Finally, we model the image formation law as follows:

$$P(y_s|x_s=\omega)\begin{cases}\frac{1}{Z_y}\frac{1}{\sqrt{2\pi}\sigma_{-1}}\exp\left[-\frac{1}{2}\left(\frac{y_s-\mu_{-1}}{\sigma_{-1}}\right)^2\right] & \text{if } \omega=-1\\ \frac{1}{Z_y}\frac{1}{\sqrt{2\pi}\sigma_1}\exp\left[-\frac{1}{2}\left(\frac{y_s-\mu_1}{\sigma_1}\right)^2\right] & \text{if } \omega=+1\end{cases} \quad (7)$$

where $(\mu_1, \sigma_1) = \arg\left[\min_{i\in\{1,2\}}\left(\frac{y_s-\mu_{1i}}{\sigma_{1i}}\right)^2\right]$

Markov modelling's constraints

It is important to note that our modeling of the image formation law is still local and does not obey to a Markovian law. Nevertheless, in a global modeling of $P(y|x)$, we can establish the most important Markov fields' properties. In fact, in hidden Markov fields' context, we can stipulate that

$$H1: P(y_s|x) = P(y_s|x_s) \quad \forall s \in S$$
$$H2: P(y|x) = \prod_{s\in S} P(y_s|x)$$

Hence:

$$P(y|x) = \prod_{s\in S} P(y_s|x_s) = \frac{1}{(Z_y\sqrt{2\pi})^{|S|}}\frac{1}{\prod_{s\in S}\sigma_{\omega(s)}}\exp\left[\sum_{s\in S}\left(\frac{y_s-\mu_{\omega(s)}}{\sigma_{\omega(s)}}\right)^2\right] \quad (8)$$

where $\omega(s)$ is the class of voxel s.

Supposing $\prod_{s\in S}\sigma_{\omega(x_s)}$ globally constant, we may express $P(y|x)$ as

$$P(y|x) = \frac{1}{Z_{yx}}\exp[-H(y,x)] \quad (9)$$

where Z_{yx} is a constant and $H(y,x)$ is the energy function defined on S.

According to Hammersley—Clifford theorem [22], (Y, X) is a Markov field. This conclusion would allow us adopting a posteriori-based decision method, as we describe it in the following section.

Estimation and decision

On the basis of the maximum a posteriori (MAP) decision method, voxels classification would consist in searching a labeling x^* that maximizes $P(x|y)$:

$$x^* = \arg\left[\max_{x\in\Omega^{|S|}}(P(x|y))\right] \quad (10)$$

According to Bayes' formula:

$$P(x|y) = \frac{P(x,y)}{p(y)} = \frac{P(x)P(y|x)}{p(y)} \propto P(x)P(y|x) \quad (11)$$

Hence, according to Eqs. (1) and (9):

$$P(x|y) \propto \frac{1}{Z_x Z_{yx}}\exp[-U(x) - H(y,x)] \quad (12)$$

The issue of loosing contrast between prostate tissues and surrounding structures at the apex and base levels is the essence of combining gray levels analysis with a priori knowledge. When implementing this method, we could notice that contours, at apex and base levels, would diverge to surrounding non-prostate voxels unless the algorithm takes in account the slice location as additional a priori knowledge; in fact, automatic segmentation would be more accurate at prostate's apex and base, if we inhibit gray levels analysis and increase the weight of prostate model-based information. To do this, we adopted a dynamic weighting parameter $\lambda(k) \in [0, 1]$ which regulates gray level-related energy function, depending on the spatial location of the voxel:

$$P(x_s|y_s) \propto \frac{1}{Z_x Z_{yx}}\exp[-\lambda(k)U(x_s) - H(y_s, x_s)] \quad (13)$$

where k is the third coordinate of the voxel $V[i, j, k]$, which corresponds in our case to the axial slice number. We modeled $\lambda(k)$ using the following mixture, which is inspired of Rayleigh's cumulative distribution function:

$$\lambda(k) = 1 - \exp\left(-\frac{k^2}{2a^2}\right) - \exp\left(-\frac{(k-n)^2}{2a^2}\right) \quad (14)$$

where a is a constant and n the number of slices ($0 \le k \le n$). Figure 3 shows the variation of $\lambda(k)$ for different values of a, and for $n = 40$ slices.

Optimization

Since it is nearly impossible to compute all labeling probabilities, we assess the MAP by the iterated conditional mode (ICM) estimator [21]. This determinist algorithm requires a relevant initialization, and consists on retaining the class that maximizes the probability $P(x_s|y)$ for each voxel:

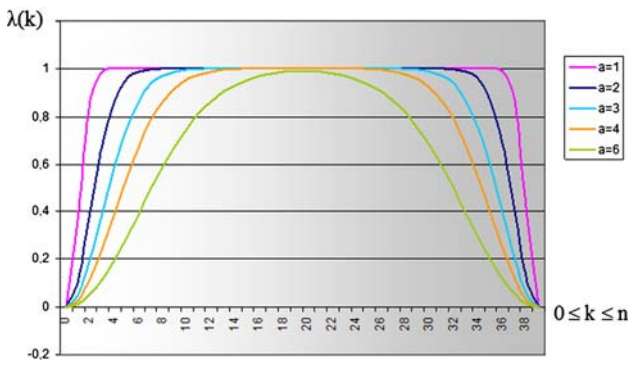

Fig. 3 Variation of spatial location-dependant weighting parameter $\lambda(k)$

$$x^* = \arg\left[\max_{x\in\Omega^{|S|}}(P(x\,|y))\right] \Leftrightarrow \begin{cases} x^* = (x_s)_{s\in S} \quad \text{so that:} \\ \forall s \in S, \quad x_s = \arg\left[\max_{x_s\in\Omega}(P(x_s\,|y))\right] \end{cases} \tag{15}$$

In addition, according to Eq. (11):

$$P(x_s\,|y) \propto P(x_s).P(y|x_s)$$

As (Y, X) and X are Markov fields, which globally means that labeling probabilities are neighborhood dependent, we are able to assume that

$$P(x_s\,|y) \propto P(x_s)P(y|x_s) \propto P(x_s|x_{V_s})P(y_s|x_s) \tag{16}$$

Hence, maximizing $P(x_s|y)$ could be done by maximizing $P(x_s|x_{Vs}).P(y_s|x_s)$. To do so, we implemented the ICM algorithm as follows:

- Initialize a first labeling map X°, using the Gibbs-sampled 3D model.
- *Repeat, for each iteration n:*
  - browse all sites and calculate for each one the conditional probability $P_n\,(x_s, y_s)$ using Eq. (13).
  - apply the following decision rule: $x_s^n = \arg\left[\text{Max}_{x_s\in\{-1,1\}}\ (P_n\,(x_s, y_s))\right]$
- *Until* $\left|x^n - x^{n-1}\right| \leq \varepsilon$

Experiments and results

The first tests were performed on 12 T2-weighted data sets obtained with Philips 1.5 T Achieva MRI device, with a voxel size of $0.83 \times 0.83 \times 4$ mm. Figure 4a illustrates the results in a large prostate, showing BPH (112 cc), for which the deformable model alone was insufficient as prostate size exceeded the generic model. Figure 4b shows a prostate with a large uniform low-intensity tumor in the right peripheral zone that mimics central zone signal, and could theoretically hinder automatic segmentation. For these tests, Markov model parameters α and β were 0.15 and 0, respectively. The weighting parameter $\lambda(k)$ was computed considering $a = 2$ (Eq. 14). The mean manual contouring time (MMCT) required for the expert radiologist on 15 slices was 17 min and 42 s (15–23 min). The mean automatic contouring time (MACT) of our algorithm on a standard 2.8 Ghz PC was 76 s (64–83 s). The method was evaluated by comparing the obtained results (free from any manual correction) to manual segmentation, performed by a senior radiologist involved in the management of prostate cancer. We measured the following parameters (V_m = manualvolume, V_a = automaticvolume):

- Hausdorff distance (HD) [22]: it is the minimal number r such that the closed r-neighborhood of V_m contains Va and the closed r-neighborhood of V_a contains V_m (optimal value = 0). In other words, if $d(V_a, V_m)$ denotes the distance in M, then:

$$d\,(V_a, V_m) = \max\left\{\sup_{x\in V_a}\inf_{y\in V_m} d\,(x, y)\,,\ \sup_{y\in V_m}\inf_{x\in V_a} d\,(y, x)\right\}$$

- Gravity distance (GD): it is the Euclidian distance between gravity centers of the two volumes (optimal value = 0).
- Overlap ratio (OR): also called Jaccard index, it is the ratio of the intersection volume of to the union volume (optimal value = 1):

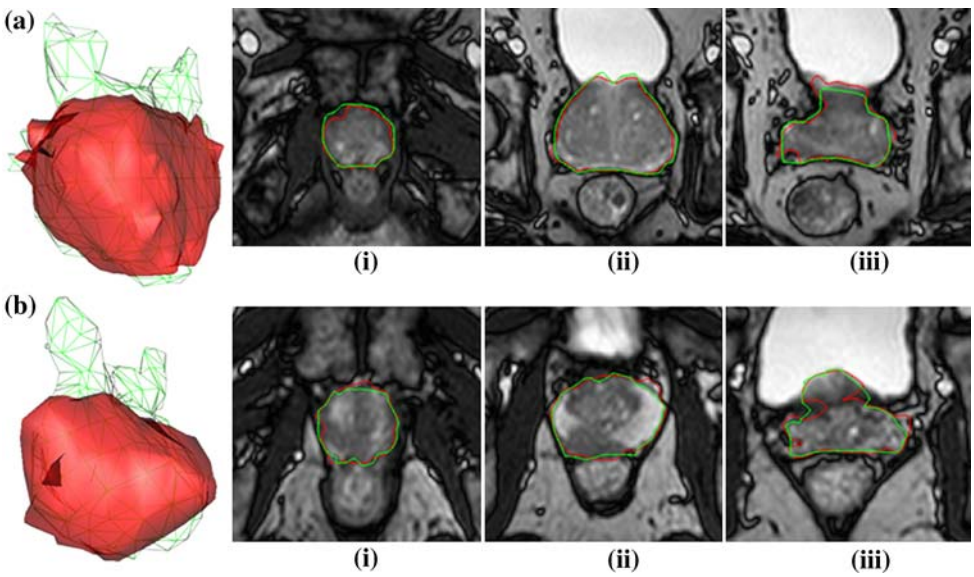

Fig. 4 Comparison of automatic contours (in *red*) and manual ones (in *green*): **a** prostate with BPH, **b** prostate with a large low intensity tumor of PZ. We present 3D visualization reconstruction, and contours at (i) apex (ii) center and (iii) base axial slices

$$\mathrm{OR} = \frac{|V_m \cap V_a|}{|V_m \cup V_a|}$$

It is important to stress that this index is very sensitive to small variations in overlap because it is normalized to the union of the volumes. As an example, if two equal volumes overlap by 85% of each, the volume overlap would be only 0.74.

- Volume properly contoured (VPC): it is the ratio of the intersection volume to the manual defined volume (optimal value = 1):

$$\mathrm{VPC} = \frac{|V_m \cap V_a|}{|V_m|}$$

- Dice similarity coefficient (DSC): it is a similarity measure related to the Jaccard index (optimal value = 1):

$$\mathrm{DSC} = \frac{2\,|V_m \cap V_a|}{|V_m| + |V_a|}$$

As one of the aims of our study is to improve previous work results [25], we computed the same coefficients for contours obtained with the active shape model (ASM). We detail full numeric results in Table 1, and we visualize difference between the two methods on diagrams of both Hausdorff's distance and dice coefficient (Fig. 5).

Discussion and conclusion

Developments in image-guided therapies increase the amount of work required for treatment planning and, in particular, for organ delineation, which is one of the most time-consuming procedures. MR delineation and TDM fusion are currently used for prostate cancer radiotherapy. CT images are primarily used for the treatment planning, but MR images are used more and more because of their soft-tissue contrast. Indeed, MRI prostate delineation allows a more accurate localization of apex and could help characterizing intra-gland structures and/or localizing suspicious tissues, in the case of tumors detection.

Different automated organ delineation methods have been studied, especially those who deal with pelvic structures. Bueno et al. [26] have presented a 2D morphologic approach based on watershed transformation for automatic rectum, bladder and seminal vesicles segmentation. A good segmentation accuracy has been reported for the tested slices (1.2–1.7 mm average distance to ground truth for bladder and rectum, respectively), but no validation of complete 3D data sets was done. Mazonakis et al. [10] have proposed a region-growing technique for the segmentation of prostate, bladder and rectum on CT images but a slider was used to define three independent threshold ranges and consequently this method cannot be considered as automatic.

In the field of prostate delineation, most of the authors consider organ model-based segmentation as a promising method [27]. Broadhurst et al. [28] in their method based on m-reps and statistical modeling of non-parametric histograms built prostate and rectum models from 17 images of a single patient. Although the approach is interesting, it remains far from the practice since it is evaluated on the same data having been used to build the models. Freedman et al. [12] combined a shape-appearance model and a probability distribution of photometric variables inside the object

Table 1 Results of comparing manual and automatic segmentation for both Markov maximum a posteriori algorithm (MMAP), and active shape model (ASM)

Sequence	HD (mm)		GD (mm)		OR		VPC		DSC	
	MMAP	ASM	MMAP	ASM	MMAP	ASM	MMAP	ASM	MMAP	ASM
1	8.0987	14.8191	3.2822	6.4021	0.8482	0.6967	0.9274	0.8026	0.9134	0.7189
2	10.2676	13.72	2.0753	3.93	0.8746	0.6824	0.9253	0.728	0.9333	0.8112
3	7.0582	11.6275	2.1834	3.5248	0.9114	0.8082	0.9569	0.8461	0.9509	0.8939
4	9.83	14.3109	2.1	3.0589	0.7866	0.7122	0.9381	0.7871	0.8805	0.8319
5	11.14	11.5342	0.67	2.4795	0.803	0.7581	0.8327	0.9585	0.8835	0.8654
6	13.28	14.95	3.73	3.9	0.8366	0.8198	0.8416	0.8552	0.911	0.901
7	8.3018	13.4953	1.5149	5.3109	0.8726	0.7596	0.9077	0.8128	0.9319	0.8633
8	8.4671	11.535	1.8684	2.1447	0.7854	0.7378	0.8968	0.7917	0.8798	0.8491
9	9.5439	16.0992	2.8791	3.8398	0.863	0.8337	0.9153	0.8654	0.9265	0.9093
10	9.4354	10.9193	2.9561	5.1033	0.869	0.7291	0.9025	0.7915	0.9299	0.8433
11	9.2115	12.4017	3.7207	4.7092	0.8147	0.7174	0.8766	0.767	0.8979	0.8354
12	10.8614	8.8236	1.7215	3.4162	0.7734	0.6856	0.9112	0.8491	0.8722	0.9134
Mean	9.6246	12.8529	2.3918	3.984	0.8365	0.7450	0.9026	0.8212	0.9092	0.8530

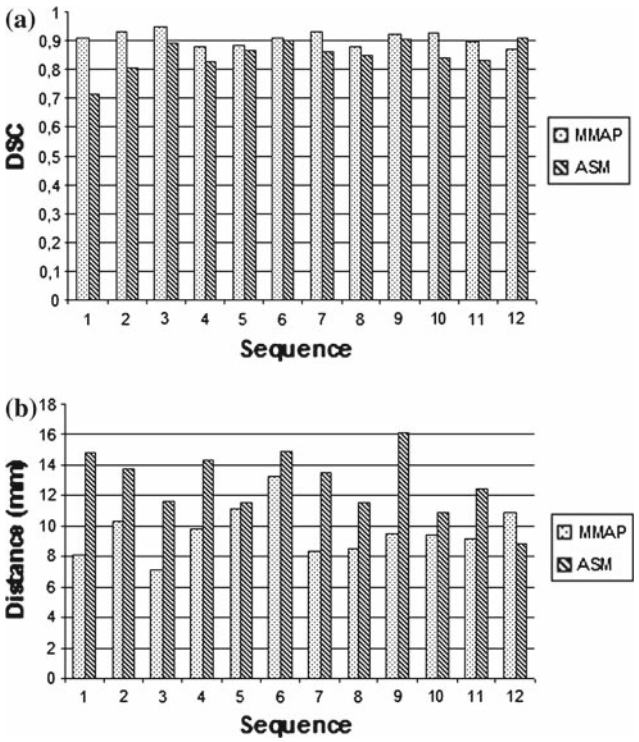

Fig. 5 Contouring performances of Markov maximum a posteriori algorithm (MMAP), and active shape model (ASM), evaluated using dice similarity coefficient (**a**) and Hausdorff's distance (**b**)

to segment the prostate and the rectum. The authors reported major user interactions to correct the results. We also noted that image registration is another major method. In Lu et al. [29] and Foskey et al. [30], the key idea was the use of the result of a deformable image registration to match two CT examinations and automatically replace manual segmentation initially laid out on the reference image. The method provides good results for intra-patient examinations but suffers of weakness for inter-patient examinations because of the assumption of conservation of voxel values. Klein et al. [11] have also recently developed a similar segmentation process by performing a non-rigid registration of a set of pre-labeled prostate atlas with the target patient images. To the best of our knowledge, Klein et al. [11] and Pasquier et al. [31] are most recent works in prostate MRI segmentation. Both authors published their results by comparing automatic contours to manual expert delineation, using DSC coefficient and overlap ratio, respectively. These evaluations showed a best DSC of 0.87 for Klein et al., and 0.88 for Pasquier et al., which means that we have better segmentation results, as shown in Table 1, even though we do not consider inter-observer variability. Moreover, the computation time, measured on a 2.8-Ghz personal computer, was around 15 min per registration for Klein et al., and 20 min for Pasquier et al., while in our method, we bring this time to less than 2 min, with the same hardware settings.

Indeed, we have developed and evaluated a new MR images anatomy automatic delineation method that combines statistical information on prostate's geometry, with a Markov field-based Bayesian segmentation. The first tests, as detailed in Table 1, show that integrating a Bayesian framework improves results previously reported by [32] when using a deformable model alone, especially at the base and the apex, where surrounding tissues are in contact with the gland and hinder the deformable model. This increased performance can be explained by the fact that our Markov field-based segmentation process relies on precise modeling of gray levels distribution that considers intra-gland structures, and avoids converging to their boundaries. On the other hand, the ICM estimator is much more rapid than both simulated annealing optimization and MRI data registration; the ICM may lead to a local *extremum*, which is not inconvenient as we have a quite good labeling initialization that is relatively close to optimal contours. Nevertheless, minor contouring errors still persist at the apex, and our method still needs to be improved at this location. It should also be evaluated on a larger set of patients, and with different sequence parameters (thinner slices, higher spatial resolution) that may improve its accuracy.

This method was designed to be part of a multi-source prostate segmentation project that will take account of other MRI sequences with different contrasts (T2-w, T1-w, etc.). Data fusion based on Evidence theory could help resolve persistent issues at the apex.

We plan to include this segmentation method in a prostate-dedicated computer-aided diagnosis (CAD) software [33] designed for localization, volume assessment and treatment planning of prostate cancer.

References

1. Fenster A, Surry K, Smith W, B Downey D (2004) The use of three-dimensional ultrasound imaging in breast biopsy and prostate therapy. Measurement 36(3–4):245–256. doi:10.1016/j.measurement.2004.09.013
2. Pekar V, McNutt TR, Kaus MR (2004) Automated model-based organ delineation for radiotherapy planning in prostatic region. Int J Radiat Oncol Biol Phys 60:973–980
3. Chaney L, Pizer S, Joshi S et al (2004) Automatic male pelvis segmentation from CT images via statistically trained multi-object deformable m-rep models. Am Soc Therapeutic Radiol Oncol (ASTRO) 60:153–154
4. McLaughlin PW, Troyer S, Berry S et al (2005) Functional anatomy of the prostate: implications for treatment planning. Int J Radiat Oncol Biol Phys 63:479–491. doi:10.1016/j.ijrobp.2005.02.036
5. Villeirs GM, Verstraete KL, DeNeve W et al (2005) Magnetic resonance imaging anatomy of the prostate and periprostatic area: a guide for radiotherapists. Radiother Oncol 76:99–106. doi:10.1016/j.radonc.2005.06.015
6. Algan O, Hanks GE, Shaer AH (1995) Localization of the prostatic apex for radiation treatment planning. Int J Radiat Oncol Biol Phys 33:925–930. doi:10.1016/0360-3016(95)00226-4

7. Roach M III, Faillace-Akazawa P, Malfatti C et al (1996) Prostate volumes defined by magnetic resonance imaging and computerized tomographic scans for three-dimensional conformal radiotherapy. Int J Radiat Oncol Biol Phys 35(5):1011–1018. doi:10.1016/0360-3016(96)00232-5
8. Lee YK, Bollet M, Charles-Edward C et al (2003) Radiotherapy treatment planning of prostate cancer using magnetic resonance imaging alone. Radiother Oncol 66:203–216. doi:10.1016/S0167-8140(02)00440-1
9. Pasquier D, Palos G, Castelain B et al (2004) MRI simulation for conformal radiation therapy of prostate cancer. Int J Radiat Oncol Biol Phys 60:636–637
10. Mazonakis M, Damilakis J, Varveris H, Prassopoulos P, Gourtsoyiannis N (2001) Image segmentation in treatment planning for prostate cancer using the region-growing technique. Br J Radiol 74:243–248
11. Klein S, van der Heide UA, Raaymakers BW, Kotte ANTJ, Staring M, Pluim JPW (2007) Segmentation of the prostate in MR images by atlas matching. In: International Symposium on Biomedical Imaging, pp 1300–1303
12. Freedman D, Radke RJ, Zhang TJ, Jeong Y, Lovelock DM, Chen CT (2005) Model-based segmentation of medical imagery by matching distributions. IEEE Trans Med Imaging 24(3):281–292. doi:10.1109/TMI.2004.841228
13. El Naqa I, Yang D, Apte A, Khullar D, Mutic S, Zheng J, Bradley JD, Grigsby P, Deasy JO (2007) Concurrent multimodality image segmentation by active contours for radiotherapy treatment planning. Med Phys 34(12):4738–4749. doi:10.1118/1.2799886
14. Costa MJ, Novelas S, Ayache N, Delingette H (2007) Automatic segmentation of bladder and prostate using coupled 3D deformable models. Med Image Comput Comput Assist Interv Int Conf Med Image Comput Comput Assist Interv 10(Pt 1):252–260
15. Pasquier D, Lacornerie T, Vermandel M, Rousseau J, Lartigau E, Betrouni N (2007) Automatic segmentation of pelvic structures from MRI images for prostate cancer radiotherapy. Int J Radiat Oncol Biol Phys 68(2):592–600. doi:10.1016/j.ijrobp.2007.02.005
16. Cootes TC, Taylor CJ (2001) Statistical models of appearance for medical image analysis and computer vision. In: Proc SPIE Medical Imaging, San Diego, CA, vol 4322, pp 236–248
17. Pasquier D, Lacornerie T, Vermandel M, Rousseau J, Lartigau E, Betrouni N (2007) Automatic segmentation of pelvic structures from MRI images for prostate cancer radiotherapy. Int J Radiat Oncol Biol Phys 68(2):592–600. doi:10.1016/j.ijrobp.2007.02.005
18. Betrouni N, Puech P, Dewalle AS, Lopes R, Dubois P, Vermandel M (2007) 3D automatic segmentation and reconstruction of prostate on MR images. Conf Proc IEEE Eng Med Biol Soc 1:5259–5262. doi:10.1109/IEMBS.2007.4353528
19. Cootes TF, Hill A, Taylor CJ, Haslam J (1994) The use of active shape models for locating structures in medical images. Image Vis Comput 12:355–366
20. Pasquier D, Lacornerie T, Vermandel M, Rousseau J, Lartigau E, Betrouni N (2007) Automatic segmentation of pelvic structures from MRI images for prostate cancer radiotherapy. Int J Radiat Oncol Biol Phys 68(2):592–600. doi:10.1016/j.ijrobp.2007.02.005
21. Besag J (1974) Spatial interaction and the statistical analysis of lattice systems. J R Stat Soc [Ser A] 36:192–236
22. Geman S, Geman D (1984) Stochastic relaxation, Gibbs distributions and the Bayesian restoration of images. IEEE Trans. Pattern Anal Mach Intell 6:721–741
23. Potts RB (1952) Some generalized order-disorder transitions. Proc Camb Philos Soc 48:106–109
24. Postaire JG, Vasseur C (1981) An approximate solution to normal mixture identification with application to unsupervised pattern classification. IEEE Trans Pattern Anal Mach Intell PAMI 3(2):163–179
25. Pasquier D, Lacornerie T, Vermandel M, Rousseau J, Lartigau E, Betrouni N (2007) Automatic segmentation of pelvic structures from MRI images for prostate cancer radiotherapy. Int J Radiat Oncol Biol Phys 68(2):592–600. doi:10.1016/j.ijrobp.2007.02.005
26. Bueno GFM, Burnham K et al (2001) Automatic Segmentation of clinical structures for RTP: evaluation of a morphological approach. MIUA '01. BMVA Press, Sheffield, pp 36–73
27. Pizer SM, Fletcher PT, Sarang J, Gash AG, Stough J, Thall A, Tracton G, Chaney EL (2005) A method and software for segmentation of anatomic object ensembles by deformable m-reps. Med Phys 32(5):1335–1345. doi:10.1118/1.1869872
28. Broadhurst RE, Stough J, Pizer SM et al (2005) Histogram statistics of local model-relative image regions. In: Olsen OF, Florack L, Kuijper A (eds) Lecture notes in Computer Science, pp 71–82
29. Lu W, Chen ML, Olivera GO, Ruchala KJ, Mackie TR (2004) Fast free-form deformable registration via calculus of variations. Phys Med Biol 49:3067–3087. doi:10.1088/0031-9155/49/14/003
30. Foskey M, Davis B, Goyal L, Chang S, Chaney E, Strehl N, Tomei S, Rosenman JS (2005) Large deformation three-dimentional image registration in image-guided radiation therapy. Phys Med Biol 50(5869):5892
31. Pasquier D, Lacornerie T, Vermandel M, Rousseau J, Lartigau E, Betrouni N (2007) Automatic segmentation of pelvic structures from MRI images for prostate cancer radiotherapy. Int J Radiat Oncol Biol Phys 68(2):592–600. doi:10.1016/j.ijrobp.2007.02.005
32. Pasquier D, Lacornerie T, Vermandel M, Rousseau J, Lartigau E, Betrouni N (2007) Automatic segmentation of pelvic structures from MRI images for prostate cancer radiotherapy. Int J Radiat Oncol Biol Phys 68(2):592–600. doi:10.1016/j.ijrobp.2007.02.005
33. Puech P, Betrouni N, Viard R, Villers A, Leroy X, Tre LL (2007) Prostate cancer computer-assisted diagnosis software using dynamic contrast-enhanced MRI. Conf Proc IEEE Eng Med Biol Soc 1:5567–5570. doi:10.1109/IEMBS.2007.4353608